

A simultaneous dual-parameter optical fibre single sensor embedded in a glass fibre/epoxy composite

Fazzi, Luigi; Valvano, Stefano; Alaimo, Andrea; Groves, Roger M.

DOI

[10.1016/j.compstruct.2021.114087](https://doi.org/10.1016/j.compstruct.2021.114087)

Publication date

2021

Document Version

Final published version

Published in

Composite Structures

Citation (APA)

Fazzi, L., Valvano, S., Alaimo, A., & Groves, R. M. (2021). A simultaneous dual-parameter optical fibre single sensor embedded in a glass fibre/epoxy composite. *Composite Structures*, 270, Article 114087. <https://doi.org/10.1016/j.compstruct.2021.114087>

Important note

To cite this publication, please use the final published version (if applicable). Please check the document version above.

Copyright

Other than for strictly personal use, it is not permitted to download, forward or distribute the text or part of it, without the consent of the author(s) and/or copyright holder(s), unless the work is under an open content license such as Creative Commons.

Takedown policy

Please contact us and provide details if you believe this document breaches copyrights. We will remove access to the work immediately and investigate your claim.



A simultaneous dual-parameter optical fibre single sensor embedded in a glass fibre/epoxy composite

Luigi Fazzi^{a,*}, Stefano Valvano^b, Andrea Alaimo^b, Roger M. Groves^a

^aStructural Integrity and Composites Group of the Faculty of Aerospace Engineering of Delft University of Technology, Delft 2629 HS, the Netherlands

^bFaculty of Engineering and Architecture, University of Enna Kore, Cittadella Universitaria, 94100 Enna, Italy



ARTICLE INFO

Keywords:

Fibre Bragg Grating
Strain
Temperature
Dual-parameter sensor
Composite
FEM

ABSTRACT

A simultaneous two-parameter single sensor based on weakly tilted Fibre Bragg Grating (TFBG), embedded in a 1 mm glass fibre/epoxy composite plate, is demonstrated to measure independently the temperature and strain variations induced in the material by the exposure to heating lamps. The spectrum of weakly TFBGs is composed of several peaks that can be used for different sensing purposes. Here, the shifting of the Bragg and the Ghost peaks are considered to calculate the strain and temperature variations through thermomechanical sensitivity coefficients of the selected peaks. To prove the reliability of the TFBG measurements, the resulting strain values were compared with the strain measurements obtained from the TFBG when compensated by a K-thermocouple embedded close to the optical fibre sensor. Furthermore, the numerical simulation of the full Finite Element Model (FEM) (composite + TFBG) and partial FEM (composite only) models were carried out by assuming a 3-D Gaussian temperature profile. This allowed the TFBG experimental measurements to be compared with the simulated results. A study focused on the strain deviation showed a good match between the full FEM and the TFBG measurements with an average error of ~5% in the case of the dual-parameter sensor and ~2% for the compensated TFBG.

1. Introduction

A short-period Bragg grating, also known as a Fibre Bragg Grating (FBG), is a permanent modulation of the refractive index (RI) induced in the core of a single-mode optical fibre (OF) with a specific profile (uniform, chirped, Gaussian, apodizing, superstructure) [1]. These OF sensors are usually embedded or surface mounted in composites and structures to provide accurate measurements without significantly increasing the weight of the components or influencing their mechanical behaviour [2]. It is well known that a single conventional FBG sensor suffers from thermomechanical cross-sensitivity, which means it is not able to uncouple the strain and temperature components of the signal [3]. Both perturbations affect the main spectral peak, called the Bragg peak, whose wavelength shift is used to calculate the magnitude of the perturbations. This drawback is a crucial point for the monitoring of the internal health state of composite materials. Therefore, to overcome this limitation, in the last decades, several FBG sensor-based monitoring technologies have been developed. The simplest proposed solutions provide FBGs written in two different OFs [3] which have different RIs and are spliced making a single waveguide, or FBGs

working at different Bragg wavelengths in a single waveguide [4]. These techniques allow the measurement of the strain and temperature variations due to the different sensitivities of the two sensors. A variation of the previous technique is the compensation of the wavelength shift induced by temperature through an encapsulated FBG used as an optical thermometer inside the composite [5]. With the same aim, the Fabry-Perot interferometer can be coupled with an FBG to discriminate strain and temperature effects [6,7]. Also, a hybrid variant called a FBG/extrinsic Fabry-Perot interferometric (FBG/EFPI) was proposed for the same scope [8]. However, this kind of solution does not supply a point (localized) measurement compromising the measurement spatial resolution and accuracy. Furthermore, the capsule which is highly intrusive can influence the mechanical performance of the material and the splices are a weak points which can induce defects inside the composite materials. Moreover, the pre-treatment steps are time consuming and may weaken the waveguides. The application of different sensors involves the use of two different kinds of interrogation systems, which means an increase of operational cost. Thermocouples (TCs) may be employed to compensate the variation of the FBG signal due to the temperature, however, these are intrusive for their large

* Corresponding author.

E-mail addresses: l.fazzi@tudelft.nl (L. Fazzi), stefano.valvano@unikore.it (S. Valvano), andrea.alaimo@unikore.it (A. Alaimo), r.m.groves@tudelft.nl (R.M. Groves).

diameter (> 1 mm). A low intrusive solution may be the use of the thin TC types as their diameter is $30\text{--}50\ \mu\text{m}$, but as experienced during the composite sample manufacturing, they are easy breakable during the embedding and de-moulding step. The discrimination can also occur through a hybrid dual sensor FBG/Long Period gratings (LPGs) as each sensor has a different sensitivity to the two parameters but this dual sensor gives back a non-localized measurement and it is very sensitive to bending [9,10].

To sum up, even if FBG sensors meet the embedding requirements, the techniques that allow the separate measurement of basic parameters such as temperature and strain suffer from some critical issues that cannot be overlooked. Therefore, a concrete solution comes from the so-called tilted FBG (TFBG) due to the imposed tilt angle to the Bragg gratings. These sensors generate a transmission spectrum with well-defined multiple resonance peaks, which may have different sensitivities to strain and temperature variations [11]. This means a single sensor provides enough information to demodulate its signal into separate strain and temperature variation measurements. Therefore each single TFBG is, at least, a dual-parameter sensor, which can be embedded in composites without another auxiliary sensor. Some previous research [12,13] was focused on the discrimination of strain and temperature variations using TFBG sensors. However, both the works are dedicated to the review of the thermo-mechanical sensitivity coefficients of selected peaks through a double calibration to build a global sensitivity matrix. Regarding the embedding, though in [14] the TFBG is embedded in a carbon fibre/epoxy composite laminate, the work is focused on the variation of the TFBG sensitivity after the embedding in composite following the wavelength shifting of the Bragg and Ghost peaks induced by well-known values of strain and temperature to the composite. Hence, basically, although the theory to uncouple the temperature-strain variations through the TFBG signal was introduced, it has not been proved yet the TFBG sensor can effectively measure the strain and temperature variations induced in a composite material from an external thermal perturbation. Therefore, this work has the aim to prove that an embedded TFBG can monitor the internal material state measuring, at the same time, the strain and the temperature variations of the material induced by an external load, which in this case is applied through heating lamps. To achieve the scope, an experiment was carried out, where a glass fibre/epoxy composite plate, with an embedded 3° tilted FBG sensor, was exposed to the heating of heating lamps. That allows inducing in the composite a simultaneous and a priori unknown variation of strain and temperature, which were measured by the TFBG sensor. Therefore, the experimental results were further compared performing a FEM simulation of the experiment where the thermal load was applied assuming a 3D Gaussian temperature distribution on the top surface of the plate.

2. TFBG sensing theory

In a conventional FBG, the core RI is permanently modulated illuminating the core layer of the OF with UV light beams passing through a periodic phase mask [1]. While, a tilted FBG is a type of short-period Bragg grating (length less than 10 mm), where the imposition of the core RI modulation is performed by tilting the phase-mask with respect to the OF or rotating the phase mask [15]. The tilted Bragg structure creates a mode-coupling system where the core forward-propagating light is coupled with the backward-propagating core mode (as in FBGs) and cladding modes. As Fig. 1 shows, part of the input light is reflected in the cladding layer where, due to total internal reflection, the modes are again redirected and coupled into the core. The energy exchange between core and cladding modes generates several resonance peaks in the spectrum at different wavelengths because each cladding mode has a different effective RI. Obviously, the tilt angle (θ) determines the coupling modes of the light and, consequently, the transmission spectrum shape.

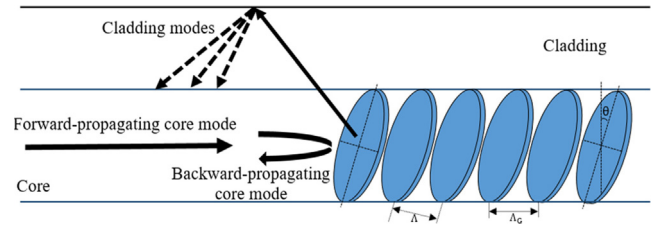


Fig. 1. Tilted FBG structure and modes propagation.

In Fig. 1, in addition to the tilt angle, two other characteristic Bragg structure parameters are defined, in particular Λ_G is the grating period along the OF axis, while $\Lambda = \Lambda_G \cos\theta$ is the nominal grating period. The Bragg and cladding peaks (λ_{Bragg} and $\lambda_{\text{clad},i}$) wavelengths can be determined from the following fundamental equations [16]:

$$\lambda_{\text{Bragg}} = 2n_{\text{eff,core}} \Lambda / \cos\theta, \quad (1)$$

$$\lambda_{\text{clad},i} = (n_{\text{eff,core}} + n_{\text{eff,clad},i}) \Lambda / \cos\theta. \quad (2)$$

where $n_{\text{eff,core}}$ and $n_{\text{eff,clad},i}$ are respectively the effective RI of the core and each i -th cladding mode. Following the theory introduced in [12], eqs.1 and 2 can be written in terms of variations by introducing the thermomechanical sensitivity coefficients. These are conventionally named as follow: $k_{\text{Bragg},\epsilon} = \partial\lambda_{\text{Bragg}}/\partial\epsilon$, $k_{\text{Bragg},T} = \partial\lambda_{\text{Bragg}}/\partial T$, $k_{\text{clad},i,\epsilon} = \partial\lambda_{\text{clad},i}/\partial\epsilon$ and $k_{\text{clad},i,T} = \partial\lambda_{\text{clad},i}/\partial T$, with ϵ and T respectively the strain and temperature. Taking into account the thermomechanical variation, the total wavelength shift of the peaks can be written as:

$$\Delta\lambda_{\text{Bragg}} = k_{\text{Bragg},\epsilon} \Delta\epsilon + k_{\text{Bragg},T} \Delta T,$$

$$\Delta\lambda_{\text{clad},i} = k_{\text{clad},i,\epsilon} \Delta\epsilon + k_{\text{clad},i,T} \Delta T. \quad (3)$$

Once the Bragg and one of the cladding resonance peaks are selected, these relations can be used together in an equations system in matrix form:

$$\begin{bmatrix} \Delta\lambda_{\text{Bragg}} \\ \Delta\lambda_{\text{clad}} \end{bmatrix} = \begin{bmatrix} k_{\text{Bragg},\epsilon} & k_{\text{Bragg},T} \\ k_{\text{clad},\epsilon} & k_{\text{clad},T} \end{bmatrix} \begin{bmatrix} \Delta\epsilon \\ \Delta T \end{bmatrix} \quad (4)$$

and solving respect the variations of ϵ and T , the direct relation is obtained:

$$\begin{bmatrix} \Delta\epsilon \\ \Delta T \end{bmatrix} = \begin{bmatrix} k_{\text{Bragg},\epsilon} & k_{\text{Bragg},T} \\ k_{\text{clad},\epsilon} & k_{\text{clad},T} \end{bmatrix}^{-1} \begin{bmatrix} \Delta\lambda_{\text{Bragg}} \\ \Delta\lambda_{\text{clad}} \end{bmatrix} = [\mathbf{K}]^{-1} \begin{bmatrix} \Delta\lambda_{\text{Bragg}} \\ \Delta\lambda_{\text{clad}} \end{bmatrix}. \quad (5)$$

Therefore, equation (5) allows the strain and temperature variations to be determined simultaneously using the inverse of the \mathbf{K} matrix, which can be also called the global sensitivity matrix, and by knowing the total wavelength shifts of the selected peaks. Though the previous mathematical treatment is referred to the Bragg and a cladding resonance, any two peaks in the spectrum can be selected and their sensitivity coefficients substituted properly in the \mathbf{K} matrix. However, the use of peaks with very different sensing behaviour allows higher temperature and strain resolutions to be achieved during the measurements as equation (6) demonstrates. From the works reported in literature [11–16], and also from the calibration step of the here used TFBG, it is noted usually all the peaks in the spectrum have substantially the same strain sensitivity coefficient. This means the key role for a proper measurement is played by the thermal sensitivity coefficient of the selected peaks. In particular, the thermal resolution (TR) can be determined from the ratio between the scanning wavelength resolution (swR) of the FBG interrogator and the absolute difference value of the thermal sensitivity coefficients, as the follow equation shows:

$$\frac{swR}{|k_{\text{peak}2,T} - k_{\text{peak}1,T}|} = TR \quad (6)$$

Hence, by increasing the difference at the denominator, a smaller TR value is obtained allowing a higher measurement resolution. TR can be also called temperature resolution of the TFBG sensing system because it depends not only on the TFBG sensor, but also on the interrogation device used to obtain the spectrum of the OF sensor.

In this work, only weakly tilted FBG sensors ($\theta < 15^\circ$) are considered as their spectrum is composed, in addition to the Bragg and the cladding peaks, of another peak called the Ghost peak [15,16]. This particular peak is the result of a group of low-order and strongly guided cladding modes coupling with the core light. It is sensitive to thermomechanical perturbations but immune, as is the Bragg peak, to surrounding RI variations, hence, it is always present in the spectrum. This is a fundamental point, as once the TFBG is embedded in the resin of the composite some cladding resonance peaks are not more visible in the spectrum as the light is irradiated out of the OF when the surrounding RI matches their effective RI [17]. Moreover, external RI variations influence also the wavelength shifting of the cladding peaks [18], this means a temperature variation causes an implicit double shifting of the cladding peaks due to the unavoidable RI changing. Therefore, a further calibration should be necessary to compensate the peak shifting caused by the RI variation from the total wavelength variation, while using the Ghost peak this is not necessary and eq.5 can be directly applied.

3. Description of the composite plate sample

The following section reports the specifications of the composite sample used for the experiment. A $170 \times 75 \times 1$ mm composite plate was made with 6 layers of unidirectional (UD) S-glass fibre and Bake-lite® Epikote 04,908 epoxy + hardener resin system, manufactured using the vacuum assisted resin transfer molding (VARTM) process and cured in the oven at 80°C for 6 h. The dimensions of the sample were correlated to those of the test chamber in the experimental setup. Moreover, the longer side was such that the dimensions had a negligible influence on the TFBG coming from the spot bonding points between OF and reinforcement layer applied during the embedding process of the OF when the sample was manufactured. The sample thickness both a good thermal stability during the experiment and ease of manufacture. A tilted FBG sensor was placed in the center of the UD composite sample at 0.5 mm height with the OF in the same direction (parallel) as the fibre reinforcement, so that to avoid possible bending effects on the sensor caused by a different orientation with the glass fibres. As the TFBG is centrally located in the plate, this position is assumed the most affected by the exposure of the heating lamps in the embedding plane, moreover it avoids boundary effects in the measurements. The tilted FBG is long 4 mm and was written in Fibercore PS1250/1500 standard-OF (cladding $\varnothing 125 \mu\text{m}$) using the tilted phase mask technique by FORC-Photonics company with a tilt angle of 3° and no coating layer for 10 mm across the length of the TFBG. Moreover, a K-type TC ($\varnothing \approx 0.3$ mm) was also placed in the same embedding plane and as close as possible to the OF sensor. However, as deeper described in the section 5 dedicated to the experiment, three others K-TCs were placed on the top and one on the bottom surface of the composite. All the TCs measurements were exploited to define the thermal boundary conditions to apply to the FEMs. Fig. 2 provides a schematic view of the sample with its dimensions and all the sensors.

4. FEM simulation

In the following section two Finite Element Models (FEMs) of the tested sample are presented. The partial model composes only by the composite plate, and the full 3D model also contains the embedded OF with the TFBG sensor. Therefore, the strain values were calculated in both the 3D models through the numerical simulation performed using Abaqus® commercial Finite Element Analysis (FEA) software.

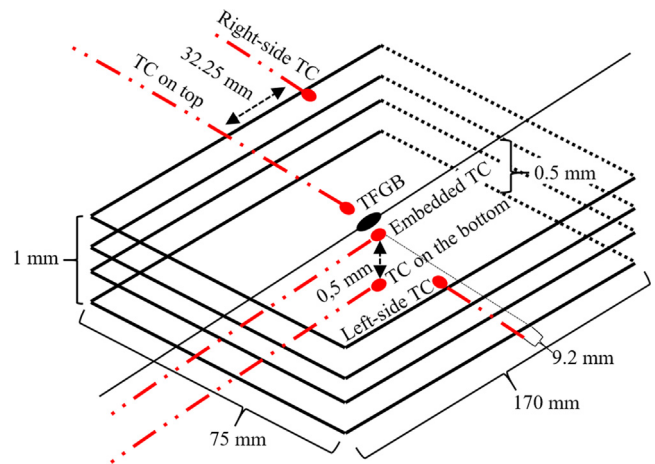


Fig. 2. Design of the composite sample with the embedded TFBG and TCs.

The FEMs are modelled by considering the composite as a homogeneous material where its thermomechanical properties are obtained from the homogenisation of those of the resin and the reinforcement fibres. While, in the full FEM, the OF is modelled considering the cladding and the core layers as a single unique cylinder covered by an external coating layer. Taking into account the nature of the experiment, the numerical simulations were performed by applying the fully coupled thermo-mechanical analysis. Therefore, since the deformations are given by solving simultaneously the heat transfer and the thermal-stress governing equations by Abaqus®, the thermomechanical properties of the resin, reinforcement fibre, OF and coating have to be considered at the same time. Hence, the density, Young and Shear modulus, and Poisson's ratio are the necessary parameters to describe the mechanical behaviour of the elements. While, the materials can be thermally characterized considering their thermal expansion, conductivity, and the specific heat coefficient.

The properties of the resin and the S-glass reinforcement fibres were provided from their respective manufacturers ([19;20], respectively), and reported in Table 1.

Regarding the FEM simulation, the first step is the calculation of the thermomechanical properties of the entire composite panel. Hence, in order to consider both the contributions of the fibres reinforcement and the resin, the relations of the composite micro-mechanical theory were used. Specifically, starting from the properties indicated from the manufacturer of the epoxy resin and glass-fibre foil, the micro-mechanical relations [21,22] were applied to obtain the homogenised composite properties. Table 2 reports the homogenised thermomechanical properties of the composite material, and also those relative to the OF and the acrylate UV-cured coating layer both available in [23], used for the FEM simulations.

Once the homogenised composite properties were obtained, the 3D FEM model of the composite plate without considering the OF (called

Table 1
Mechanical properties of the resin and S-glass reinforcement fibres.

Mechanical properties	Resin [19]	S-glass fibre[20]
Density ($\text{kg} \cdot \text{m}^{-3}$)	1150	2490
Young Modulus (GPa)	2.9	89
Shear Modulus (GPa)	0.98	37
Poisson's Ratio	0.35	0.22
Thermal properties		
Thermal expansion coefficient (K^{-1})	63.1×10^{-6}	2.85×10^{-6}
Thermal conductivity coefficient ($\text{W} \cdot \text{K}^{-1} \cdot \text{m}^{-1}$)	0.25	1.25
Specific heat coefficient ($\text{J} \cdot \text{K}^{-1} \cdot \text{kg}^{-1}$)	1000	737.5

Table 2
Mechanical properties for the FEM simulation of the materials used in the experiment.

Mechanical properties		Composite (homogenised)	OF [23]	Coating[23]
Density ($\text{kg} \cdot \text{m}^{-3}$)	ρ	1954	2300	1100
Young Modulus (GPa)	E_1	54.56	73.1	3.1
	E_2	13.32		
	E_3			
Shear Modulus (GPa)	G_{12}	2.356	31.5	1.7
	G_{13}			
	G_{23}	3.13		
Poisson's ratio	ν_{12}	2.72×10^{-1}	0.16	0.36
	ν_{13}			
	ν_{23}	2.584×10^{-6}		
Thermal properties				
Thermal expansion coefficient (K^{-1})	α_1	4.131×10^{-6}	5.5×10^{-7}	7.8×10^{-5}
	α_2	3.504×10^{-5}		
	α_3			
Thermal conductivity coefficient ($\text{W} \cdot \text{K}^{-1} \cdot \text{m}^{-1}$)	κ_1	8.5×10^{-1}	1.4	0.189
	κ_2	6.679×10^{-1}		
	κ_3			
Specific heat coefficient ($\text{J} \cdot \text{K}^{-1} \cdot \text{kg}^{-1}$)	c_v	842.5	703	1360

as partial-model), was built-up in ABAQUS and meshed using 3D elements C3D20RT with reduced integration and thermo-mechanical capabilities. The modelled plate is shown in Fig. 3a and b, where the mechanical boundary conditions are applied on the bottom surface and in the corners. In particular, each point of the bottom (Fig. 3a) is constrained such that the mechanical displacements through z -direction of the surface ($z = 0$) is not allowed ($w_i = 0$) to simulate the composite plate resting through a metal support plate during the experiment. Moreover, since some layers of Kapton-tape were placed on the corners to hold the composite plate in position, then their displacements along the three directions are imposed to be zero ($u = v = w = 0$), as shown in Fig. 3b. All the other points of the model are free to move along the spatial directions as no further constraints are applied on the sample.

The results of the partial model allowed to obtain a better understanding of the OF interactions with the surrounding composite material during the heating lamps exposure. Furthermore, the comparison between the simulation results of the two models and the TFBG measurements prove the importance of including the OF in the FEM model to obtain the correct values. Based on the previously partial model, the Full 3D FEM model was made by adding the OF embedded in the plate and placed along the direction of the glass fibre reinforcement, in the middle of the plate at half thickness (Fig. 4) of the composite sample (Fig. 2).

The Fibercore PS1250/1500 OF, introduced in section 3, is protected by an external coating protective layer of UV-cured acrylate (diameter 254 μm). The coating layer was removed before of the TFBG embedding for 10 mm across the length of the sensor, in this way the thermomechanical perturbations affect directly the no-recoated sil-

ica material of the OF. Regarding the FEM simulation, the OF was modelled in the same way, in particular, the waveguide is covered by the coating layer for the whole plate length, except for a centre region of 4 mm (where the TFBG is placed), which is directly in contact with the epoxy resin (as shown in Figs. 5a, b and 6). Finally, the partial plate model discretization was performed using 94,064 global elements, with 4 elements through its thickness and, considering the TFBG position (missing in the partial model), 12 elements were adopted in correspondence of the sensor length where the axial deformations were evaluated. While, the full model was discretized with 300,650 elements. In particular, the section plane (y,z) of the OF was modelled using 3 elements along it and the coating layer radius. As shown in Fig. 3, a more dense mesh was used in correspondence of the TFBG length. Specifically, here, the section of the OF and composite panel were discretized with 12 elements along the x -direction from which the axial strains are obtained. While, the remaining sections sides in correspondence of the bare OF, in the proximity of the TFBG, were modelled with 4 elements.

Regarding the thermal boundary conditions, the measurements of the TCs mounted on top of sample during the experiment (reported in the section 5) were exploited to obtain the temperature profile of both the FEMs. However, though the temperature magnitudes are known at each 3 secs based on the position of the TCs, the spatial distribution of the temperature in the plate is unknown as well as the exposure beam profile of the heating lamps. Therefore, considering the wave nature of the light and the TCs measurements, the first thermal boundary condition was applied using a temperature distribution profile on the surface of the modelled plates, represented by a Gaussian spatial distribution (Eq.7).

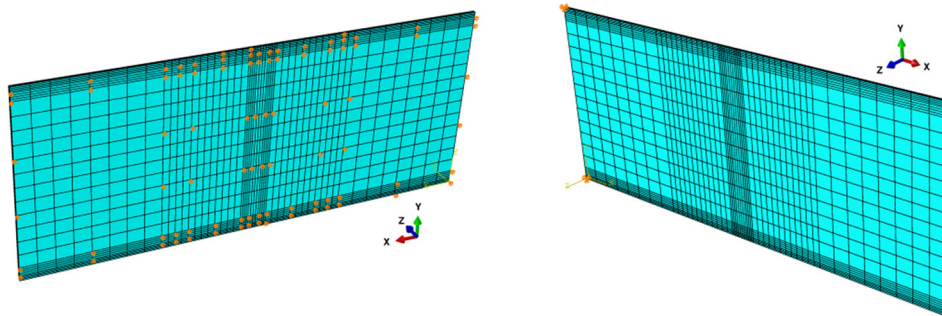


Fig. 3. Mechanical boundary conditions on the (a) bottom surface and (b) corners of the upper surface.

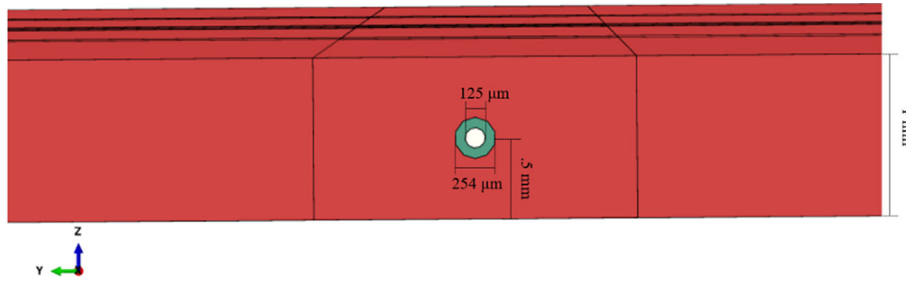


Fig. 4. Plate section of the full model, considering the OF (in white) and the coating layer (in green).

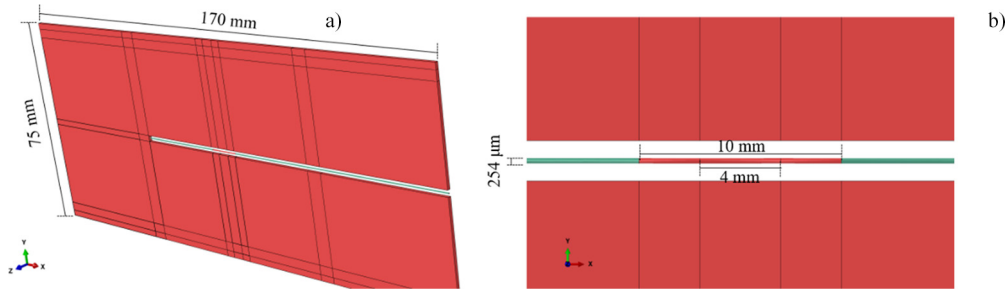


Fig. 5. Section view of (a) the whole plate with the inserted OF with coating and (b) zoomed centred region.

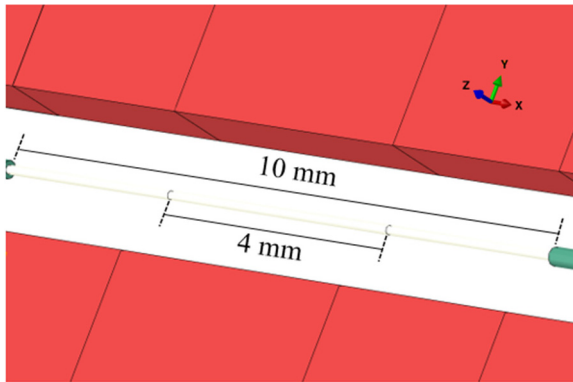


Fig. 6. No re-coated optical fibre section in the central plate region.

$$T(x,y,z_{top},t) = T_0(t) \left(\frac{\Delta T_{maxE}}{\Delta T_{maxC}} \right) + \left(\frac{T_{st}}{\Delta T_{maxC}} \right) e^{-\left(\gamma(x-a/2)^2 + 2(x-a/2)(y-b/2) + \eta(y-b/2)^2 \right)} \quad (7)$$

where the nominal temperature T_0 is the temperature amplitude obtained from the TCs during each acquisition time during the exposure. In eq.7, the coordinates x , y and z are the directions along the main axes of the plate and t is the experiment (or exposure) time which can be considered as time increments. Regarding the coefficients, a is the longer and b shorter in-plane dimensions of the sample, while ΔT_{maxE} and ΔT_{maxC} are the maximum temperature variations, respectively at the edge and top centre of the plate, respect with the starting temperature of the experiment (T_{st}). While, γ and η are coefficients used to control the shape of the Gaussian profile; these were obtained through an iteration process aimed to reach the same temperature values of the Gaussian profile in correspondence of the coordinates of the three TCs on top of the plate. Another thermal boundary condition was applied by taking into account the temperatures measured by the TCs embedded inside the composite (Fig. 2) and on the bottom surface of the plate. Indeed, when processing the experimental data, a negative

temperature gradient of $2 \pm 0.3^\circ\text{C}$ through the thickness of the plate was noted. Therefore, a $2^\circ\text{C}/\text{mm}$ linear temperature gradient through the thickness is imposed on both the 3D FEMs. Therefore, though the thermal properties of the materials were introduced in the models and, hence, the temperature can be calculated in each point of the plate, the experimental data from the TCs shown a different trend of the temperature through the thickness. As deeper treated in the next sections, this effect is caused by the air cooling system of the facility where the experiment was performed. The air vortex effects generated by the fan of the cooling system is not modelled explicitly in the simulations but it is implicitly considered through this second boundary condition. Following the applied thermal boundary conditions, Fig. 7 shows the temperature distribution profile on the upper surface of the modelled composite plate when the maximum variation is achieved during the entire exposure. Since the Gaussian profile distribution is dependent from t , this evolves starting from the beginning of the experiment at $t = 0$ as the temperature T_0 changes with the time increments during the experiment. Furthermore, due to the second thermal boundary condition, the temperature profile evolves through the thickness with the

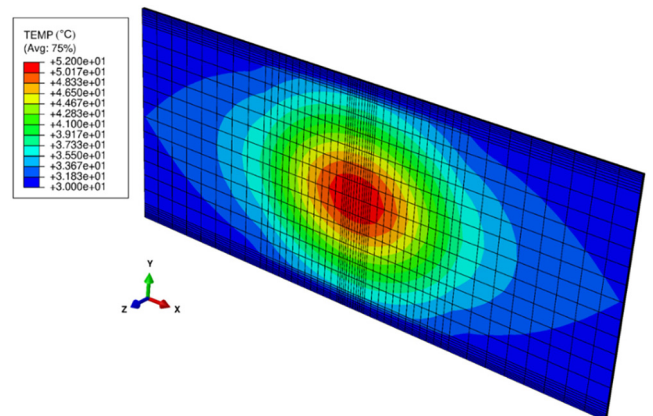


Fig. 7. Temperature distribution on the top surface of the composite plate when the maximum temperature variation is achieved.

same distribution but with a negative gradient of $2\text{ }^\circ\text{C}/\text{mm}$. Once completed the modelling steps, the FEM simulations of the partial and full 3D model were solved using the coupled steady-state thermo-mechanical analysis at each time increment, which were defined by the TCs acquisition time.

5. Experiment

As described in the previous theory section, the sensitivity coefficients of the Bragg and Ghost peak must be found experimentally before the embedding of the TFBG. With this aim, the TFBG was calibrated in two separate calibration steps using a dedicated linear translation stage and a heating plate. All the specifications regarding the setup used for the calibration are reported in Appendix A. Fig. 8a and b show the wavelength variation trends of the Bragg and Ghost peaks caused by the increasing of the strain and temperature imposed on the TFBG sensor.

The strain calibration graph (Fig. 8a) shows the sensor behaviour following of a strain perturbation is substantially linear for both the peaks. The obtained nominal strain sensitivity coefficient for the Bragg peak is $1.255\pm 0.004\text{ pm}/\mu\epsilon$ and $1.255\pm 0.006\text{ pm}/\mu\epsilon$ for the Ghost resonance with a square error (R^2) of 0.999962 and 0.999968 respectively. Also in Fig. 8b, the variation trends of the peaks with the temperature increasing are substantially linear but with different gradients. Considering the slope of the two linear trends, the thermal sensitivity coefficients obtained are $k_{\text{Bragg},T} = 9.114\pm 0.007\text{ pm}/^\circ\text{C}$ and $k_{\text{Ghost},T} = 9.6\pm 0.01\text{ pm}/^\circ\text{C}$ where R^2 are respectively 0.99888 and 0.99809. Therefore, considering swR of the interrogator system (value reported in Appendix A) in eq.6, a temperature resolution $TR\approx 8.23\text{ }^\circ\text{C}$ is obtained. Once the calibration step was done, the TFBG sensor was ready to be embedded between the composite layers during the manufacturing of the sample as was introduced in section 3.

Once cured, the composite sample was placed on a metallic plate with threaded holes, hence, as anticipated in the previous sections, other K-TCs were applied in different points to record the temperature. The accuracy of the TCs is $\pm 1^\circ\text{C}$. In particular, one of these TCs was taped on top of the sample with some Kapton tape, while the other two were screwed at the sides of the sample, Fig. 9 shows a zoomed view of the sample where all the sensors are present.

The metallic plate with on top the composite sample was collocated inside a test chamber, which is from above exposed to the light of 2 heating lamps (max. $2\times 1000\text{ W}$) placed inside a case. Moreover, the chamber was provided of an air cooling system arranged through a fan that introduces fresh air into the cylindrical duct to avoid over-

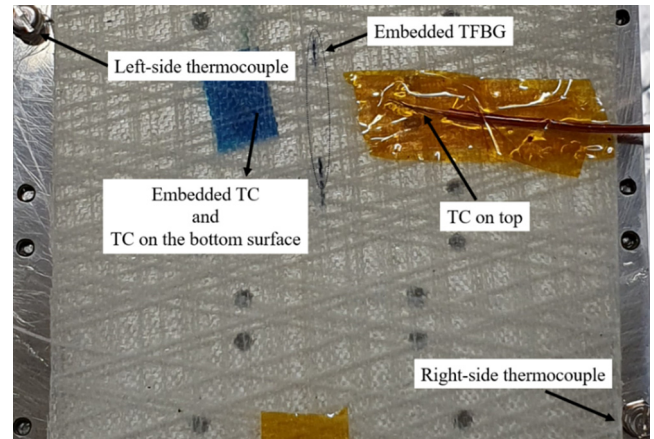


Fig. 9. Zoomed in top view of the sample on the test metallic plate with all the sensors positions marked.

heating of the experimental setup components. The airflow propagates through the entire case and streams out through a special duct. Fig. 10 shows a schematic of the experimental setup. The optical fibre enters and exits the test chamber through special holes, and was connected to an optical circulator and, hence, to the interrogator system, which, via a dedicated LabView program, was arranged to acquire the TFBG spectra automatically during the experimental tests.

6. TFBG Strain-Temperature measurements

In this section, the strain and temperature variations of the composite material during the exposure are presented. These are obtained from the TFBG measurements used as a single dual-parameter sensor and a strain gauge OF sensor compensated with TC readings. The transmitted spectrum of the embedded TFBG is shown in Fig. 11, where the Bragg, Ghost and cladding peaks are indicated. A dedicated algorithm were developed to identify the Bragg and Ghost peaks by exploiting their lower amplitudes compared to the other peaks. Once the two lowest amplitudes are detected then their correspondent wavelengths can be easily obtained, this process is applied to each spectrum recorded during the experiment. Hence, the wavelength variations $\Delta\lambda_{\text{Bragg}}$ and $\Delta\lambda_{\text{Ghost}}$ can be easily calculated between any two spectra along the acquisition time. The starting point here is considered to be the turning-on of the heating lamps, which corresponds in

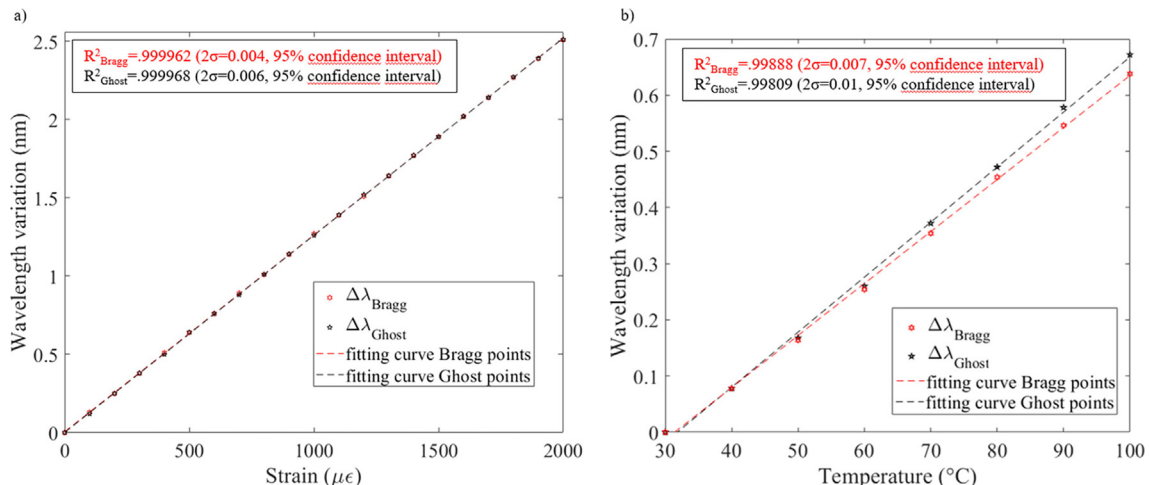


Fig. 8. Bragg and Ghost peaks shifting with a) strain and b) temperature increasing.

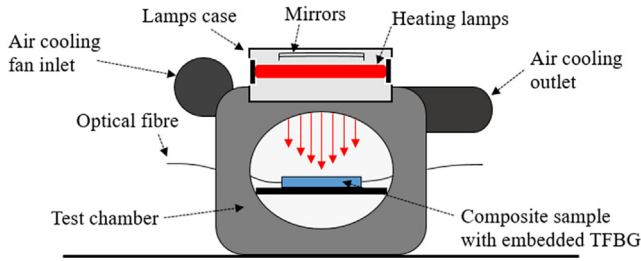


Fig. 10. Schematic of the experimental setup used to perform the exposure on the composite sample.

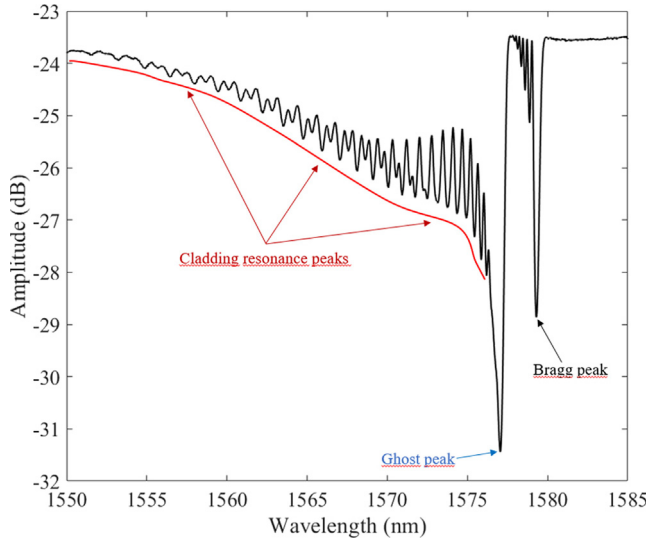


Fig. 11. 3° tilted FBG transmission spectrum with the main peaks marked.

the graphs to zero time ($t = 0$). Therefore, the strain or temperature trends have to be considered as variations in the material with respect to the origin condition at $t = 0$.

At this point, since the K matrix is known from the TFBG calibration, the matrix product between K^{-1} and the vector of the wavelength shifts (eq.5) allows the strain and temperature changes to be obtained in the materials between any two different times during the experiment. Since the strains are evaluated along the optical axis of the OF across the TFBG length, this is the x -direction and, the deformation is indicated with ε_{xx} .

In Fig. 12 the shifts of the Bragg and Ghost wavelength caused by the heating of the lamps is reported along with the exposure time, starting from $t = 60$ (at the end of the heating up phase). As expected, the wavelength shift variation of the Ghost peak is greater than the Bragg peak because of its larger temperature sensitivity coefficient of the first.

After heating up the sample with the lamps (~60 min), small temperature changes were detected by the TCs, however, as the TFBG system has a $TR \approx 8.23$ °C, the sensor is not able to detect these temperature variations. Hence, in these cases, the strain state is calculated in isothermal conditions, this means the strain evaluation could be over- or under-estimated. For this reason, to verify the TFBG measurements, the embedded TC was used to compensate the temperature effect on the Bragg wavelength variation of the TFBG, and then to obtain the strain value using the TFBG as a standard FBG. In Fig. 13, the measurements of temperature and strain calculated with the TFGB are shown with the temperature trend detected by the embedded TC. Substantially, the comparison between the strain extents measured with the TFBG and TFBG + TC compensation reach a better match

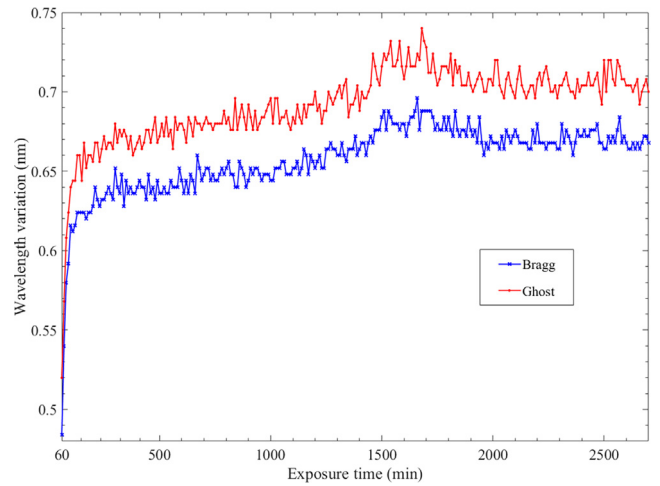


Fig. 12. Wavelength shift variation of the Bragg and Ghost peak along the exposure time.

as the temperature curves are close. This is demonstrated in Fig. 14 where the percentage deviation of the strain values is reported by considering that the TFBG measurements are performed by a single sensor and are compensated after the heating-up step (56 min). In particular, starting from a larger deviation at the beginning of the graph, when the temperature curves are separated enough, the percentage goes down with the approach of the TC measurement to that of the TFBG. The minimum deviation (0.098%) is measured at 1240 min (as the vertical blue dashed line indicates) because at this time the temperature curves intersect each other. While, as the deviation increases (the strain curves move away from each other, Fig. 13) when the TC records a temperature variations in correspondence of the oscillations between ~1500 min and ~1800 min. While the last part of the graphs confirms that the deviation and, hence, the distance between the strain curves (in Fig. 13) is proportional to the separation of the temperature curves. The difference between the strain curves obtained using the TFBG sensor singly or compensated is due to the temperature resolution of the TFBG sensing system (TR). In fact, the variations smaller than TR are not visible to the TFBG using the demodulation technique represented by eq.5. This means that the wavelength variations of the selected peaks caused by temperature changes smaller than TR , are mathematically assumed as strain variations. Hence, the calculation could return an over- or under-evaluated strain state based on the TR and the temperature. Referring to Fig. 13, the TFBG strain values result then under-estimated until ~1200 min because the isothermal calculation is performed with a temperature higher than the more accurate one measured through the embedded TC. While, in the interval between ~1500 and ~1800 min, the temperature of the TC is greater than the one measured with the TFBG, consequently, the strain values indicated by the TFBG are over-evaluated. In the other intervals time, the strain curves can be considered almost coincident with a deviation below 3%.

7. FEA results and comparison with experimental measurements

Another main point of this work is the comparison of the experimental results with the strain trends resulting from the FEM simulations of the partial and the full 3D models. The axial strain (ε_{xx}) of the material is considered to be along the modelled OF axis in correspondence and across the length of the TFBG sensor. In the case of the partial model, since the OF is not present, ε_{xx} are considered along the same length and position of the TFBG as if the OF were embedded. In Fig. 15 the strain values calculated from the simulation of the partial model are shown and compared with the TFBG measurements. A sub-

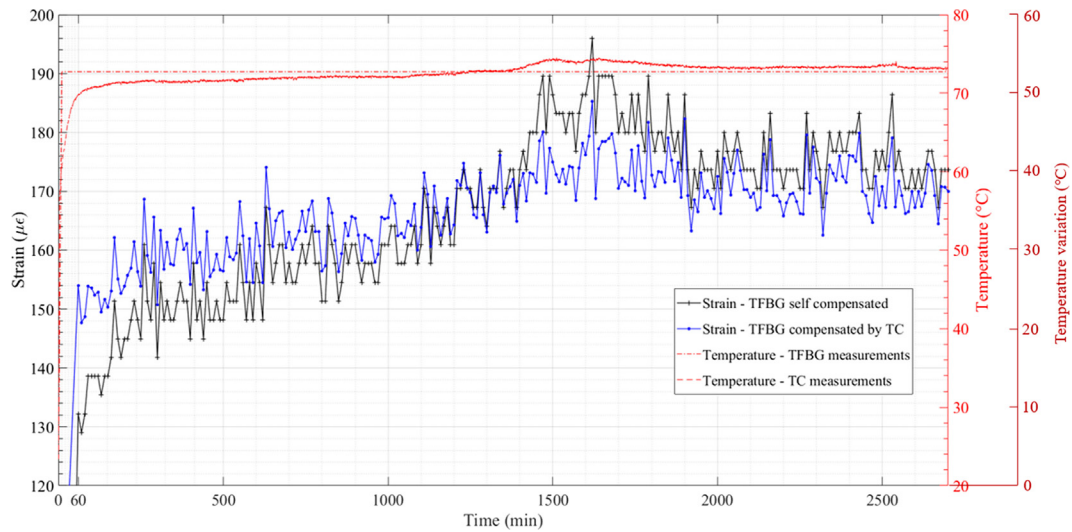


Fig. 13. Strain and temperature trends obtained in the case of single TFBG sensor measurement and TFBG with TC compensation.

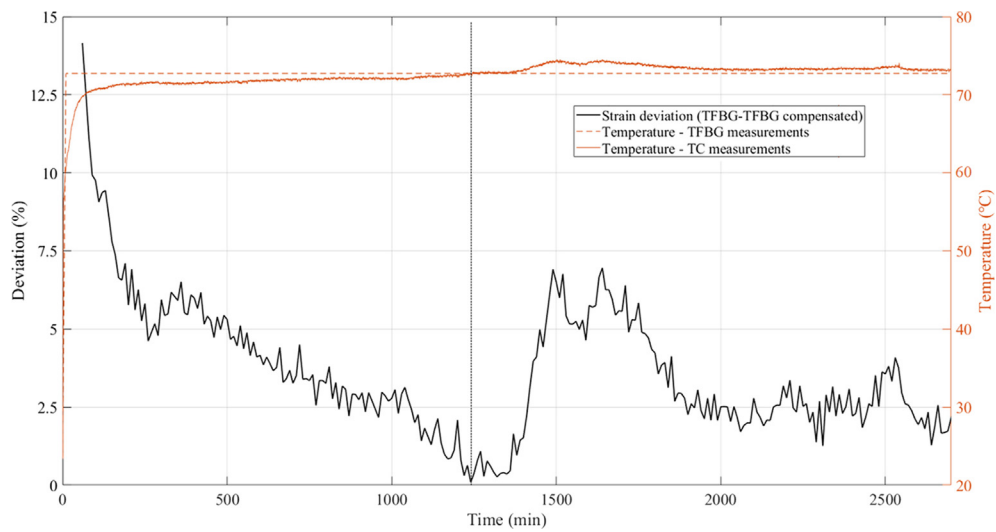


Fig. 14. Deviation between the strain measured with the embedded TFBG as a dual-parameter sensor and that compensated with the TC.

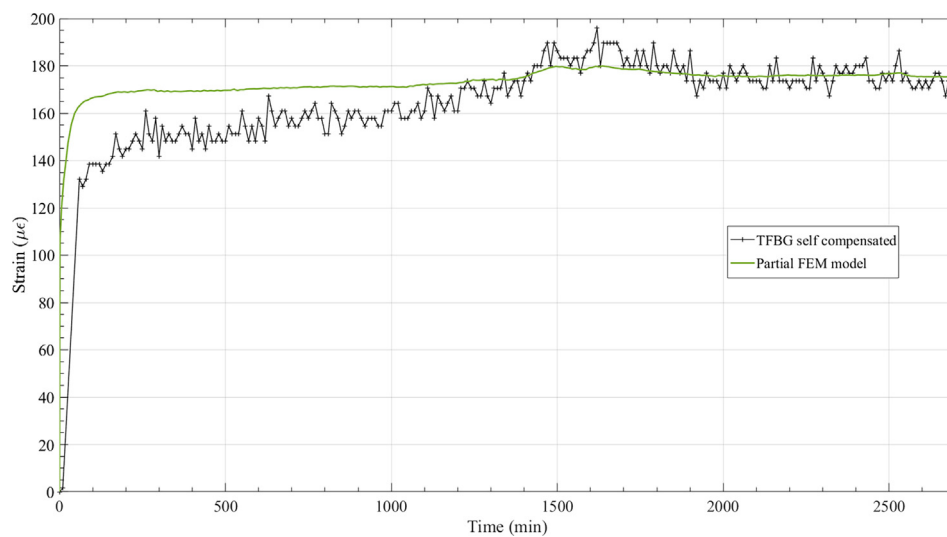


Fig. 15. Measured strain comparison between dual-parameter TFBG sensor and partial model FEA.

stantial difference between the ε_{xx} curves of the partial and measured with the dual-parameter TFGB sensor can be noted at the beginning of the experiment, during the temperature rise of the composite material due to the heating by the lamps, and then tend to be more similar starting from 1200th minute. However, the missing the OF in the partial model can slightly influence the local behavior of the material and this is demonstrated from the FEA processed on the full model and reported below.

As described in section 4, the full model includes of the composite plate with the embedded OF covered by the coating layer except across, the length of the TFGB where it is removed. The ε_{xx} obtained numerically from the simulation of the full model are reported in Fig. 16 with those of the partial model and the strain curves of the experimental measurements (Fig. 13) performed with the TFGB sensor. The ε_{xx} values are considered, even in the full model, to be along the axial direction of the OF and measured across the TFGB length. While, regarding the calculation error of the numerical simulations, the strain values of Fig. 16 were compared with those obtained performing the FEA where the same FEMs (described in section 3) were discretised by a mesh with 50% of the elements. A strain difference lower than 0.5% was obtained for each time increment. Hence, since the here considered strain values are obtained from the FEMs with a higher number mesh elements, the error was considered negligible.

The strain curve obtained from the FEA of the full FEM model (in Fig. 16) is visibly lower respect with that of the partial model. This behaviour is due to the higher stiffness of the full model for the presence of the OF, which has a higher Young's and Shear modulus than the composite plate (Table 2). For this reason, after the heating-up phase, the two curves have the same trend but they are constantly separated by $\sim 6\mu\epsilon$ ($\sim 3\%$). This proves that the OF embedding does not influence negatively the composite mechanical performance but, rather, the OF presence inside the material should be always modelled to obtain proper results from the numerical simulations. Therefore, the full model, resulting stiffer than the partial one, it shows a strain trend closer to the TFGB measurements, especially if the TFGB is compensated by the TC. This is demonstrated in the next section focused on the error analysis between the experimental and the simulations results.

8. Error analysis

To quantify the deviation obtained between the experimental and simulation results, the percentage error of the FEM models curves with

respect the TFGB strain measurements were calculated starting from the 60th exposure minute (in which the heating step is considered over). Fig. 17a and 17b report these deviations respectively for the TFGB as a single dual-parameter sensor and the TFGB compensated with TC measurements. As expected from Fig. 16, the lowest strain error trend is obtained when comparing the full model simulation results with the compensated TFGB measurements. While, especially in the first part of the graphs, the partial model returns a consistent deviation with respect with the strain experimentally measured through the TFGB using both the techniques. In general, it is also possible to note that the deviations are higher when considering the comparison with the TFGB applied as single dual-parameter sensor. Moreover, in Fig. 17a, at the time interval starting from 1320th minute, the partial model curve reaches lower error percentages than the full model one. This is an unexpected behaviour that could be misleading. In fact, when considering the single TFGB sensor measurements reported in the graph in Fig. 16, at the same time, the black curve raises-up for the effect of a positive temperature variation, so that it is measuring strain values closer to those obtained from the partial model simulation respect with the full model one. This is an inconvenience linked to the TR value of the TFGB sensing system. Indeed, since temperature variations (between any two temporal points) smaller than the TR are not taken into account in the strain calculation using the demodulation technique represented by eq.5, the contribution to the wavelength shifting of the peak is assigned to a strain perturbation. For this reason, as was anticipated from Fig. 13 (and Fig. 14), the strain trend measured by the single TFGB deviates upwards from the full model and TFGB compensated curves. This once again underlines the necessity to reduce the TR value of the TFGB sensing system, and hence, to adopt an FBG interrogator device with a finer SWR or a particular customization of the TFGB sensor that increases the difference between the temperature sensitivity coefficients of the selected peaks. These modifications would allow a finer measure of the temperature variation from the selected peaks of the TFGB spectra to be obtained. Consequently, the obtained mechanical response is more accurate using the single TFGB as a dual-parameter OF sensor without the compensation of a further sensor. As a last consideration, when considering the error of the FEA full model result with respect to the TFGB measurements in Fig. 17a and b, the average deviation along the exposure time is $\sim 5.3\%$ and $\sim 2.7\%$ respectively in the case of single dual-parameter and compensated TFGB sensor. Translating these percentages into strain values by considering the maximum deformation obtained from

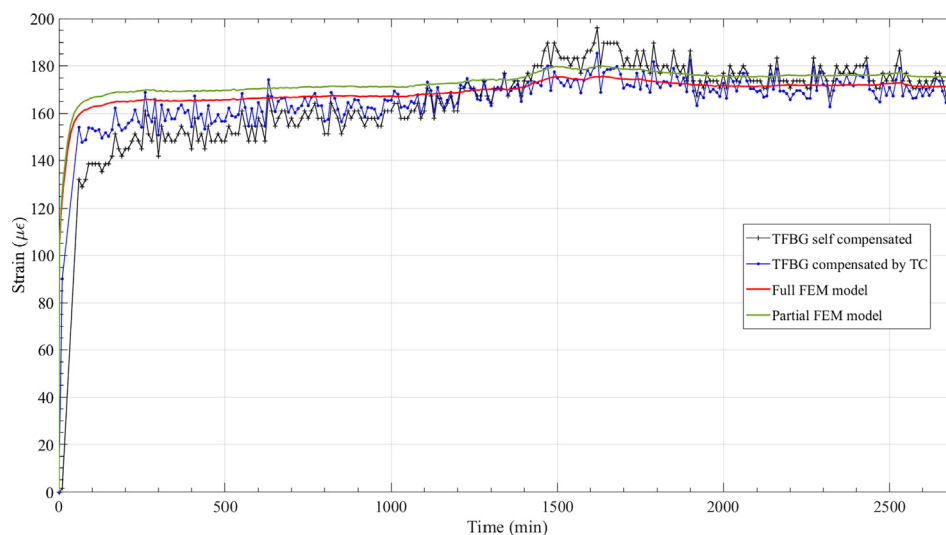


Fig. 16. Comparison between the numerical and experimental results.

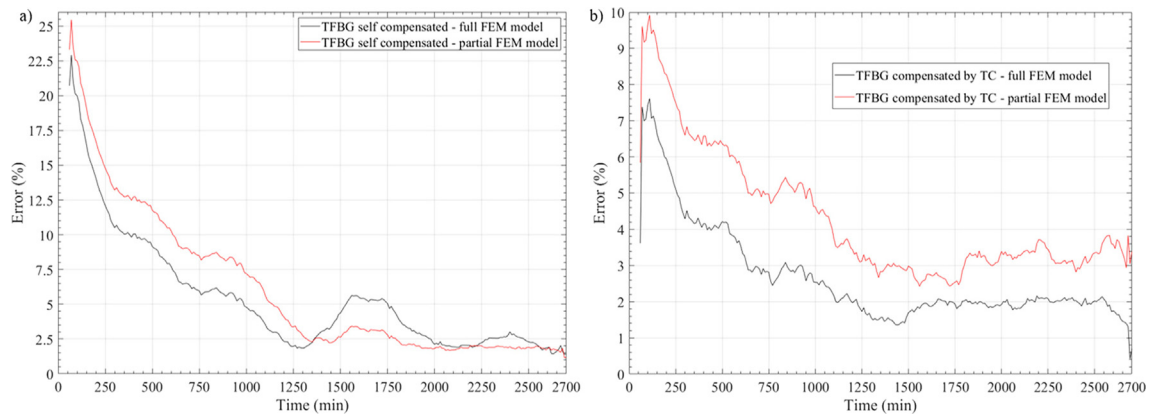


Fig. 17. Strain error comparison between the full and partial FEM models respect with the TFBG measurements performed as (a) single dual-parameter and (b) external temperature compensated sensor.

both the TFBG measuring techniques, gives deviations of $\sim 10 \mu\epsilon$ and $\sim 5 \mu\epsilon$.

9. Discussion

Some final considerations regarding the experimental measurements, the simulation results, the spatial distribution of the temperature in the FEAs and the experimental setup are reported here to conclude the discussion of the work.

In section 6, the main reason of the difference between the strain variations obtained with the TFBG as single dual-parameter sensor and compensated by the TC, was identified in the TFBG thermal resolution (TR). This drawback can be overcome by considering an interrogation system with a smaller scanning wavelength step or a special customization of the Bragg grating structure of the TFBG, such as to increase the difference between the thermal sensitivity coefficients (k_T) of the two selected peaks. A smoother temperature resolution capacity of the TFBG allows a more accurate temperature-strain calculation removing the need to assume the isothermal condition. However, despite the TR here achieved, the maximum strain difference or deviation between the strain (blue and black) curves obtained, after the heating-up of the lamps (which is a critical phase), corresponds at $\sim 14.2\%$ ($\sim 22 \mu\epsilon$) at 60 min, while the average strain deviation of all the measurements is 3.4% ($\sim 5 \mu\epsilon$). Therefore, in conclusion after this comparison, the TFBG used as single dual-parameter optical sensor appears to be a valid tool for the embedded measuring of strain and temperature, though its accuracy can be improved decreasing its TR value.

Considering the achieved results from the numerical simulations and the comparison of these with the experimental results, it is possible to confirm that the Gaussian spatial distribution of the temperature assumed in the FEAs properly describes the thermal conditions of the plate during the heating, but only after the initial warming-up phase. A possible physical explanation for this initial deviation is that at the beginning the temperature distribution is different from the assumed one as the heat generated by the lamps on the composite is partially conducted to the metallic test plate on which the sample is placed. Furthermore, each lamp needs a certain time (4–6 h, depending from the power level and environmental test conditions) to switch on and give stable irradiation power. This lag is not the same and homogeneous among the lights, hence the full operational condition is reached differently for each lamp and that can influence the initial spatial distribution of the temperature on the sample. Moreover, also the air cooling system certainly influences the temperature profile as it increases the dissipation of the heat from the composite to the environ-

mental elements (air, metallic test plate and walls). In particular, the air cooling system is composed by an external fan that aspirates the air at room temperature and accelerates it in the test chamber from which, after the interaction with the several elements, it is extracted through a special duct. Hence, the air cooling effect is not uniform on the surface of the composite as the air vortex changes its own thermal and kinematics conditions from the ingress to the outlet of the chamber. The created FEM models do not take into account all these phenomena, but, the imposed temperature profile is not perturbed or modified during the simulation time. As consequence, the assumed temperature profile distribution in the FEM models may differ from the real one during the exposure time. A further consequence of this high heat dissipation concerns the temperature gradient inside the composite plate. In fact, a preliminary comparison between the simulated temperatures (obtained through the thermal properties of the material) and the TCs measurements on top, middle and bottom of the composite sample, show a substantial difference. Therefore, to consider this effect in the simulations, a second boundary condition was imposed to the FEAs through a thermal gradient through the thickness obtained from the TCs temperatures.

Although all the previous factors can influence the effectiveness of the assumed Gaussian spatial distribution of the temperature in the FEAs, as Fig. 17a and b summarize, the average deviation (or strain error) between the experimental measurements performed with the TFBG sensor and the full 3D model is small enough to have a good match for the great part of the exposure time. As expected from the issues introduced previously, the higher strain errors are detected at the beginning of the exposure, as close to the warming-up phase. The execution of the FEM simulation in steady-state analysis could be another possible cause of the difference between the numerical and experimental results. Since the high temperature gradient during the short heating-up phase, a transient analysis could be more appropriate to simulate the model until the 60th minute. However, this interval is very short compared with the total exposure time, hence, unless the transient interval is relevant, the same kind of analysis is not convenient to simulate in the FEM model.

10. Conclusions

In this paper, a single embedded TFBG sensor, in a glass fibre/epoxy composite plate, is demonstrated to be able to measure simultaneously and separately temperature and strain during the exposure to heating lamps. A TC was also embedded close to the OF sensor in order to compare the temperature values with those measured by the single TFBG and obtain the strain variations from the sensor used as a FBG

compensated. Overall, as the deviation trends show, a good match is obtained between the strain curves of the TFBG used as single dual-parameter and compensated sensor, especially after the warming-up phase. However, this comparison highlights the drawback of the TFBG used as single dual-parameter OF sensor due to the strong influence of the temperature sensitivity coefficients of its selected peaks, which define the temperature resolution of the measuring system. This limitation can be solved using an interrogation system with a finer wavelength scanning resolution or a specific TFBG customization. However, to perform a proper TFBG customization in order to obtain certain sensing characteristics, is a hard and time consuming process, while the use of a more powerful interrogator system is an easier and more suitable, albeit expensive, strategy.

Partial (only composite sample) and full (sample + embedded TFBG) FE models were constructed to simulate the experiment and to obtain the strain trend by applying a 3D Gaussian temperature distribution on the top surface and through the composite plate. The numerical simulations demonstrated that they are able to provide the same trends as the TFBG measurements after the warming-up phase. The strain trend of the full FEM model appears to overlap well the strain values measured with the single TFBG sensor (average deviation $\sim 5.3\%$), though, as the error analysis shown, it returns a lower error when compared with the TFBG compensated measurements (average deviation $\sim 2.7\%$). However, as widely discussed in section 9, the assumed temperature profile used for the simulation is not appropriate during the first phase of the experiment. The comparison of the simulation results of the partial and full FEM with the TFBG measurements proves the low intrusiveness of the sensor and that it does not influence the mechanical performance of the composite, however it is recommended to model the OF into the FEM composite model to confirm the accuracy of the model.

In conclusion, it is possible to affirm that a single dual-parameter TFBG sensor was proved to be effective to measure simultaneously and separately strain and temperature during the exposure of heating lamps, though its measurement accuracy can be increased adopting technical stratagems to the temperature resolution.

This technique is specifically useful for dual-parameter measurements in applications where low intrusiveness is required and/or a minimum number of sensors should be used. A suitable example is the TFBG embedding through the thickness of thick composites to monitor their state during the manufacturing process. This allows the strain and temperature level in several points of the thick composites to be obtained without affect their mechanical performance. Furthermore, a future development of this technique is its integration and simultaneous running with the surrounding RI measurement. This would allow not only the thermomechanical state of the material surrounding the TFBG to be detected, but also its chemical changes.

CRediT authorship contribution statement

Luigi Fazzi: Resources, Conceptualization, Methodology, Software, Formal analysis, Data curation, Investigation, Writing - original draft, Visualization. **Stefano Valvano:** Methodology, Software, Formal analysis, Data curation, Validation, Writing - original draft. **Andrea Alaimo:** Supervision, Project administration. **Roger M. Groves:** Supervision, Visualization, Project administration.

Declaration of Competing Interest

The authors declare that they have no known competing financial interests or personal relationships that could have appeared to influence the work reported in this paper.

Acknowledgement

We would like to thank our colleague Dmitrii Klyukin for his contribution in choosing the best TFBG sensors customization, and his comments and suggestions during the preparation of this paper. This research was supported by the Operationeel Programma Zuid-Nederland (Op-Zuid) Project as part of the Dutch Composite Maintenance Centre (DCMC), supported by the Europees Fonds voor Regionale Ontwikkeling (EFRO) and the North Brabant province of the Netherlands.

Appendix A

The sensor was interrogated with a 4-Channel NI PXI-4844 Universal Input Module based on Fabry-Pérot tunable filter technology able to scan, with 4 pm of scanning wavelength resolution along a range between 1510 nm and 1590 nm. For the strain calibration of the TFBG sensor, the optical fibre, with the sensor in the middle point, was mounted on a dedicated linear translation stage composed by two extreme side blocks and a metallic guide. One of the blocks holds OF while the other one pulls it through an electric linear actuator with 2 μm of relative accuracy. The metallic guide, used like a bridge, allows the alignment of the two blocks and the OF to be maintained. For the thermal calibration step, a heating plate was used to warm up the OF in which the TFBG is placed on the translation stage (Fig. A1). The heating device has a controller that provides the temperature reading with an accuracy of $\pm 2^\circ\text{C}$. The temperature range considered for the calibration is from 30°C until 100°C . The spectra were recorded each 10°C and the temperature was double checked with a second K-type TC (accuracy $\pm 1^\circ\text{C}$.) placed adjacent to the TFBG. Moreover, an isolation foam was used on top of the setup to minimize the heat dispersion and to create uniform environment conditions. The

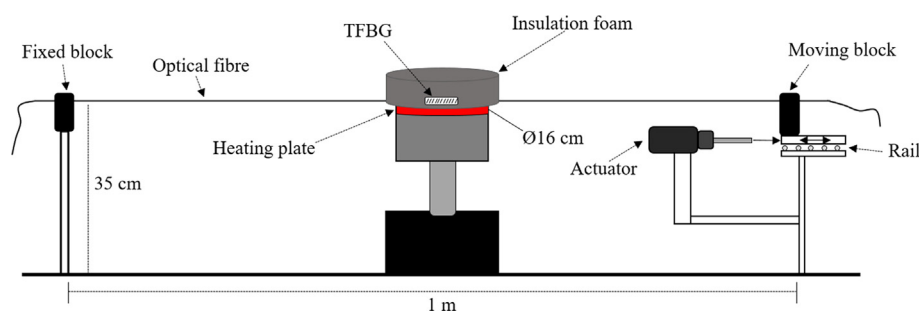


Fig. A1. A schematic of the translation stage and heating plate used for the thermomechanical calibration of the TFBG sensor.

translation stage was also used to hold the OF aligned and in position during the thermal calibration, and a pretension of 185 μm was applied to the TFBG before starting the calibration.

References

- [1] Erdogan T. 'Fiber grating spectra'. *J Lightwave Technol* 1997;15(8):1277–94.
- [2] Luyckx G, Voet E, Lammens N, Degrieck J. 'Strain Measurements of Composite Laminates with Embedded Fibre Bragg Gratings: Criticism and Opportunities for Research'. *Sensors* 2011;11(1).
- [3] Cavaleiro PM, Araujo FM, Ferreira LA, Santos JL, Farahi F. 'Simultaneous Measurement of Strain and Temperature Using Bragg Gratings Written in Germanosilicate and Boron-Codoped Germanosilicate Fibers'. *IEEE Photonics Technol Lett* 1999;11(12):1635–7. <https://doi.org/10.1364/OL.27.000701>.
- [4] Shu X, Liu Yu, Zhao D, Gwandu B, Floreani F, Zhang L, et al. 'Dependence of temperature and strain coefficients on fiber grating type and its application to simultaneous temperature and strain measurement'. *Opt Lett* 2002;27(9):701. <https://doi.org/10.1364/OL.27.000701>.
- [5] Montanini R, D'Acquisto L. 'Simultaneous measurement of temperature and strain in glass fibre/epoxy composites by embedded fibre optic sensors: I. Cure monitoring'. *Smart Mater Struct* 2007;16:1718–26.
- [6] de Oliveira R, Ramos CA, Marques AT. 'Health monitoring of composite structures by embedded FBG and interferometric Fabry-Perot sensors'. *Comput. Struct.* 2008;86(3–5):340–6.
- [7] Kang HK, Kang DH, Bang HJ, Hong CS, Kim CG. 'Cure monitoring of composite laminates using fibre optic sensors'. *Smart Mater Struct* 2002;11(9):279–87.
- [8] Kang H-K, Kang D-H, Hong C-S, Kim C-G. 'Simultaneous monitoring of strain and temperature during and after cure of unsymmetric composite laminate using fibre-optic sensors'. *Smart Mater Struct* 2003;12(1):29–35.
- [9] Patrick HJ, Williams GM, Kersey AD, Pedrazzani JR, Vengsarkar AM. 'Hybrid fibre Bragg grating/long period fibre grating sensor for strain/temperature discrimination'. *Photonics Technology Letters* 1996;8(9):1223–5.
- [10] Triollet S, Robert L, Marin E, Ouerdane Y. 'Discriminated measures of strain and temperature in metallic specimen with embedded superimposed long and short fibre Bragg Gratings'. *Meas Sci Technol* 2011;22(1):015202. <https://doi.org/10.1088/0957-0233/22/1/015202>.
- [11] Chen C, Caucheteur C, Mégret P, Albert J. 'The sensitivity characteristics of tilted fibre Bragg grating sensors with different cladding thicknesses'. *Meas. Sci. Technol.* 2007;18:3117–22.
- [12] Chehura E, James SW, Tatam RP. Temperature and strain discrimination using a single tilted fibre Bragg grating. *Opt Commun* 2007;275:344–7.
- [13] Dong B, Hao J, Liaw C, Lin B, Tjin SC. Simultaneous strain and temperature measurement using a compact photonic crystal fiber inter-modal interferometer and a fiber Bragg grating. *Appl Opt* 2010;49(32):6232–5.
- [14] D. Kinet, D. Garraay, P. Mégret, C. Caucheteur, "Temperature and strain effects discrimination inside composite materials with embedded weakly tilted fibre Bragg grating", *Proceedings of SPIE*, 87942R1 – 6 (2013).
- [15] Albert J, Shao L-Y, Caucheteur C. 'Tilted fiber Bragg grating sensors'. *Laser Photonics Rev* 2013;7(1):83–108.
- [16] Alberto NJ, Marques CA, Pinto JL, Nogueira RN. 'Three-parameter optical fiber sensor based on a tilted fiber Bragg grating'. *Appl Opt* 2010;49(31):6085. <https://doi.org/10.1364/AO.49.006085>.
- [17] Fazzi L, Groves RM. Demodulation of a tilted fibre Bragg grating transmission signal using α -shape modified Delaunay triangulation. *Measurement* 2020;166:108197. <https://doi.org/10.1016/j.measurement.2020.108197>.
- [18] Chan C, Chen C, Jafari A, Laronche A, Thomson DJ, Albert J. Optical fiber refractometer using narrowband cladding-mode resonance shifts. *Appl. Opt.* 2007;46(7):1142–9.
- [19] Hexion technical information. <https://www.swiss-composite.ch/pdf/t-Hexion-Harz-EPR04908.pdf>; (last access 22/02/2021).
- [20] AZOMaterials. <https://www.azom.com/properties.aspx?ArticleID=769>; (last access 22/02/2021).
- [21] Chamis CC. *Mechanics of composite materials: past, present and future*. *J. Compos. Technol. Res.* 1989;11:3–14.
- [22] Struzziero G, Nardi D, Sinke J, Teuwen JJE. Cure-induced residual stresses for warpage reduction in thermoset laminates. *J. Compos. Mat.* 2020:1–11.
- [23] Fibercore technical information. <https://fibercore.humaneticsgroup.com/products/photosensitive-fiber/boron-doped-photosensitive-fiber/ps12501500>; (last access 22/02/2021).